PAPER

Carrier-doping and strain driven tuning of magnetic properties in the p-orbital monolayer metal-free ferromagnet T-XN$_2$ (X = Sb, Bi)

Jiajun Zhu, [ID][a] Guangsheng Liu*[b] and Duohui Huang*[a]

Two-dimensional non-metallic ferromagnetic states have attracted widespread attention due to their complete spin polarization, long spin relaxation times, and abundant availability, highlighting their potential applications in next-generation spintronic devices. Based on first-principles calculations, we predict the two-dimensional non-metallic ferromagnet T-XN$_2$ (X = Sb, Bi), which has a structure similar to T-MoS$_2$. Calculations of thermodynamic, kinetic, and mechanical properties confirm that they possess good stability. Spin polarization results indicate that the ground state of monolayer T-XN2 is ferromagnetic, with its magnetism arising from the direct p-orbital interactions between N atoms, unlike conventional d/f orbital magnetic materials. Furthermore, the ferromagnetism retains good stability under strain engineering and carrier doping. These results suggest that the magnetic properties of monolayer T-XN$_2$ hold significant fundamental research implications and make it a potential candidate material for non-metallic ferromagnetic devices.

1 Introduction

Spin, as a degree of freedom, has attracted significant attention due to its advantages in high storage density, substantial data processing capabilities, and low power consumption, which have contributed to the development of spintronics.[1,2] The growing demand for performance necessitates the development of new ferromagnetic materials that exhibit high abundance, complete spin polarization, and elevated Curie temperatures.[3,4] Recently, following the successful experimental synthesis of the two-dimensional ferromagnetic semiconductor CrI$_3$,[5] several two-dimensional magnets have been synthesized using techniques such as exfoliation and carrier doping, including Cr$_2$Ge$_2$Te$_6$,[6] FeSn,[7] Fe$_3$GeTe$_2$,[8] VSe$_2$,[9] and others.[10] Current research primarily focuses on developing potential two-dimensional magnets characterized by abundant availability, lightweight, high durability, non-toxicity, and high stability.[11] In particular, metal-free two-dimensional materials composed of main group elements have attracted significant attention.[12] Main group elements typically demonstrate weaker spin–orbit coupling than transition metals, leading to longer spin lifetimes.[13] This phenomenon is attributed to the relatively weak spin–orbit coupling effects within their p-electron systems, which enhances their potential for applications in spintronics, particularly in biocompatible devices and electronic equipment.[14] However, traditional metal-free two-dimensional magnets impose stringent requirements for defect engineering and functionalization, complicating operations for experimentalists.[15] Therefore, the search for metal-free two-dimensional ferromagnets that possess excellent spin properties and electronic characteristics simultaneously holds significant theoretical value and offers promising practical applications.

Recently, the layered magnetic material H-MoN$_2$ has been successfully synthesized, attracting significant attention due to its structural similarity to H-MoS$_2$.[16] Researchers refer to this nitrogen-rich structure as transition metal dinitrides (TMN$_2$). Theoretically, H-MoN$_2$ is predicted to be a ferromagnetic metal with a Curie temperature above room temperature (420 K).[17] Upon hydrogenation, it undergoes a phase transition to the T-MoN$_2$ phase structure, which features a Dirac cone.[18] Both T-YN$_2$ and T-TaN$_2$ exhibit characteristics of ferromagnetic semimetals. T-YN$_2$ is a room-temperature p state Dirac semimetal, whereas T-TaN$_2$ has a larger semimetal bandgap (0.72 eV) that prevents spin flipping.[19] Additionally, Chen *et al.* systematically predicted H-phase and T-phase transition metal dinitrides using high-throughput calculations, identifying 87 potentially viable materials and studying their stability.[20] In contrast to the aforementioned transition metal dinitrides, main group dinitrides are theoretically predicted to exist in T-PN$_2$ and T-AsN$_2$,[21,22] which exhibit ferromagnetic semimetal characteristics, with magnetism derived from the p orbitals of nitrogen atoms. However, related compounds, SbN$_2$ and BiN$_2$, have not yet been reported. Therefore, we are interested in the magnetic and electronic structures of the remaining V-group dinitrides, specifically T-SbN$_2$ and T-BiN$_2$.

[a]School of Mathematics and Physics, Computational Physics Key Laboratory of Sichuan, Yibin University, Yibin, 644000, China. E-mail: hdhzhy912@163.com
[b]School of Materials and Energy, Yunnan University, Kunming, 650091, P. R. China

Based on this background, we predicted the main group magnetic nitrides T-XN$_2$ (X = Sb, Bi), and investigated their stability and magnetic properties. Through phonon dispersion, first-principles molecular dynamics, and mechanical property analysis, we confirmed that they exhibit good stability. Spin-polarized calculations show that the ground state of mono-layer T-SbN$_2$ and T-BiN$_2$ is ferromagnetic, with their magnetism originating from the p-orbitals of the N atoms, where each N atom contributes a magnetic moment of 0.5 μ_B. Additionally, calculations indicate that the effects of strain engineering and carrier doping on the magnetic properties are highly robust. These results suggest that monolayer T-SbN$_2$ and T-BiN$_2$ are potential candidates for two-dimensional non-metallic spin-tronic materials.

2 Method

First-principles calculations were performed based on density functional theory as implemented in the Vienna *Ab initio* Simulation Package (VASP).[23–25] The electron–electron interactions were treated within a generalized gradient approximation (GGA) in the form of Perdew–Burke–Ernzerhof (PBE) for the exchange-correlation functional.[26,27] We take the energy cutoff 650 eV and the thickness 15 Å for vacuum. The criteria were set to 10^{-8} eV and 10^{-5} eV Å^{-1} for energy and force with the $18 \times 18 \times 1$ Monkhorst–Pack sampling for self-consistent calculations, respectively. The phonon dispersion is performed based on density functional perturbation theory (DFPT) as embedded in the Phonopy program.[28] The phonon dispersion using $4 \times 4 \times 1$ supercell. Phonon dispersion and molecular dynamics simulations are both performed under the assumption that the system is ferromagnetic. The calculation of the total magnetic energy does not include SOC, whereas T_c – related parameters, such as the magnetic exchange coefficient J, MAE, and magnetic properties tuned by carrier doping or strain, we have take SOC into account. The mechanical properties are computed without considering SOC, using the VASPKIT software to calculate the energy–strain curves,[29] and the quadratic term coefficient is obtained by fitting.

3 Results and discussion

The relaxed crystal structure is shown in Fig. 1(a), which consists of three atomic layers of N–X–N occupying positions A, B, and C, respectively. Its structure is similar to that of 1T-MoS$_2$, with each unit cell consisting of three atoms, sharing the space group $P\bar{3}m1$ (No. 164) with a nonpolar point group D_{3d}. The optimized lattice constants $a = b$ are 3.378 Å and 3.491 Å for 1T-SbN$_2$ and 1T-BiN$_2$. The X atom is located at the midpoint of the line connecting two layers of N atoms and is bonded to six equivalent N atoms. The bond length X–N are 2.19 Å (Sb–N) and 2.30 Å (Bi–N), and the vertical height between the two N atoms are 1.99 Å (SbN$_2$) and 2.20 Å (BiN$_2$). The bonding properties of the XN bond can be characterized by Bader charge and the Electron Localization Function (ELF). The calculation results of the Bader charge show that electrons were transferred from the X atom to the N atom, with a 1.05 e per N atom (SbN$_2$) and 0.87 e
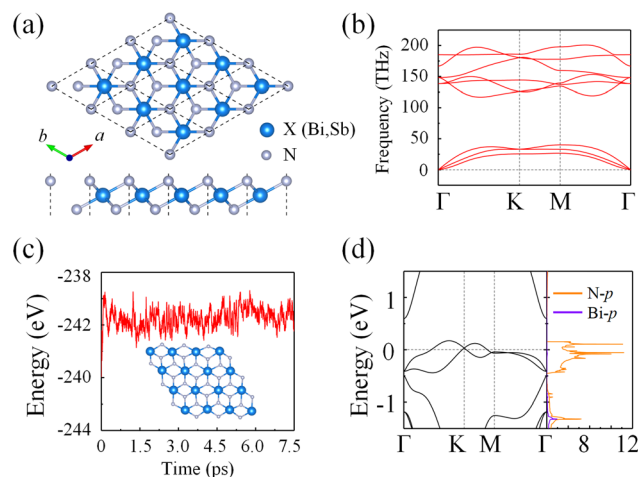

Fig. 1 Crystal structure information. (a) Top view and side view of T-XN$_2$. (b) Phonon dispersion of T-BiN$_2$. (c) AIMD of T-BiN$_2$ with 0−7.5 ps. (d) Band structure and projected density of states for the non-magnetic state of T-BiN$_2$.

per N atom (BiN$_2$). We calculated the ELF along the $(hkl) = (110)$ plane, which is displayed in Fig. S1 in the SI. The ELF map shows that electrons are primarily localized around each atom, with only a small amount of electrons existing between the X–N bonds, indicating that the X and N atoms are connected by a weak covalent bond. The above evidence suggest that the X–N bond in monolayer 1T-XN$_2$ is a weak covalent bond. This result is similar to the bonding properties of V–V group compounds that we know.

The stability of the material can be demonstrated through mechanical stability, dynamical stability, and thermodynamic stability. In addition, we have taken into account the ferro-magnetism of the material in all calculations related to stability proof. The elastic modulus are typically used to represent the ability of materials to resist deformation and can be used to characterize the mechanical stability of the materials. The elastic modulus of 2D materials can be expressed as:

$$C = \frac{1}{A}\frac{\partial^2 E}{\partial \varepsilon^2} \tag{1}$$

here, A, E and ε represents the area of unit cell, the strain total energy and in-plane uniaxial strain. The second-order elastic modulus matrix of a two-dimensional hexagonal lattice material with space group $P\bar{3}m1$ can be expressed using three elastic constants, denoted as C_{11}, C_{12}, and C_{66}. The calculated results are listed in Table 1.

The three elastic modulus values of T-SbN$_2$ are all greater than those of T-BiN$_2$, indicating that monolayer T-SbN$_2$ is softer

Table 1 Structural information parameters for lattice constant a (Å), bond length $l_{Ti–X}$ (Å), Bader charge ΔQ (e) and elastic constants (N m^{-1})

Materials	a	$l_{Ti–X}$	ΔQ	C_{11}	C_{12}	C_{66}
1T-SbN$_2$	3.378	2.19	1.05	97.2	48.8	29.3
1T-BiN$_2$	3.491	2.30	0.87	66.4	32.0	15.9

than monolayer T-BiN$_2$ and more suitable for applying strain to modulate its physical properties. In addition, the mechanical stability of the 2D hexagonal lattice can be determined by the Born–Huang criterion,[30] which must satisfy the $C_{11}C_{22} > C_{12}^2$ and $C_{66} > 0$. We further examine whether the monolayer T-XN$_2$ material satisfies the above formula, and the results show that they are mechanically stable.

Phonon dispersion is often used to characterize dynamic stability, and the phonon dispersion of monolayer T-XN$_2$ is presented in Fig. 1(b) and S2 in SI. The calculation results show that all acoustic and optical branches are greater than zero, demonstrating that monolayer T-XN$_2$ is dynamically stable. Furthermore, increasing atomic mass lowers the total phonon energy and increases the band gap between the optical and acoustic branches.

The thermodynamic stability is confirmed by the AIMD simulation of the material's total energy variation over a finite time period.[31,32] We simulated the total energy variation of monolayer T-XN$_2$ over 7.5 ps, and the results are presented in Fig. 1(c) and S2 in SI. The calculation results show that the structure at the end of 300 K remains essentially unchanged except for a slight twist, and the total energy fluctuation of the supercell does not exceed 24 meV per atom. The degree of distortion in the structure is represented by the root mean square displacement $\bar{d} = \frac{1}{N}\sum_{i=1}^{N}(l_i - l_0)$ between the X–N bonds, where l_i and l_0 represent the bond lengths during AIMD simulations and the bond lengths when not simulated,

respectively. The calculated root mean square displacement $\bar{d}$ values are 0.05 Å and 0.09 Å, indicating that the monolayer T-XN$_2$ are thermodynamically stable at room temperature.

The band structure of non-magnetic T-BiN$_2$ is presented in Fig. 1(b), clearly showing that there are energy bands cross the Fermi level, indicating a metallic state. Two energy bands intersect at the K point, forming a Dirac cone similar to that of single-layer graphene. These two energy bands are primarily composed of the p$_z$ orbitals of nitrogen. The density of states and the shape of the energy bands exhibit characteristics reminiscent of a Mexican hat, suggesting that a magnetic phase transition may occur in monolayer T-BiN$_2$

The electron distribution of N and Bi are $2s^2 2p^3$ and $6s^2 6p^3$, respectively, making them non-magnetic elements belonging to group V. However, when the Bi atom in the middle layer bonds with the N atoms in the upper and lower layers, the Bi atom will lose 3 electrons from its outer 6p orbital. The N atoms in the upper and lower layers each gain one electron, filling the p$_x$ and p$_y$ orbitals along with their original 2p orbitals.[21,22] As a result, the net magnetic moment of the system is 1 μ_B, with each N sharing a magnetic moment of 0.5 μ_B. The spin-polarization calculation shows that monolayer T-BiN$_2$ exhibits ferromagnetic state with a magnetic moment of 1 μ_B per unit cell. The spin-polarized density map in Fig. 2(b) indicates that the magnetism originates from the p orbitals of the N atoms. The spin-polarized energy bands are shown in Fig. 2(e), where the two degenerate bands near the Fermi level are split, resulting in channels for spin-up and spin-down, while retaining the Dirac cone at the K point. The projected density of states in Fig. 2(b)
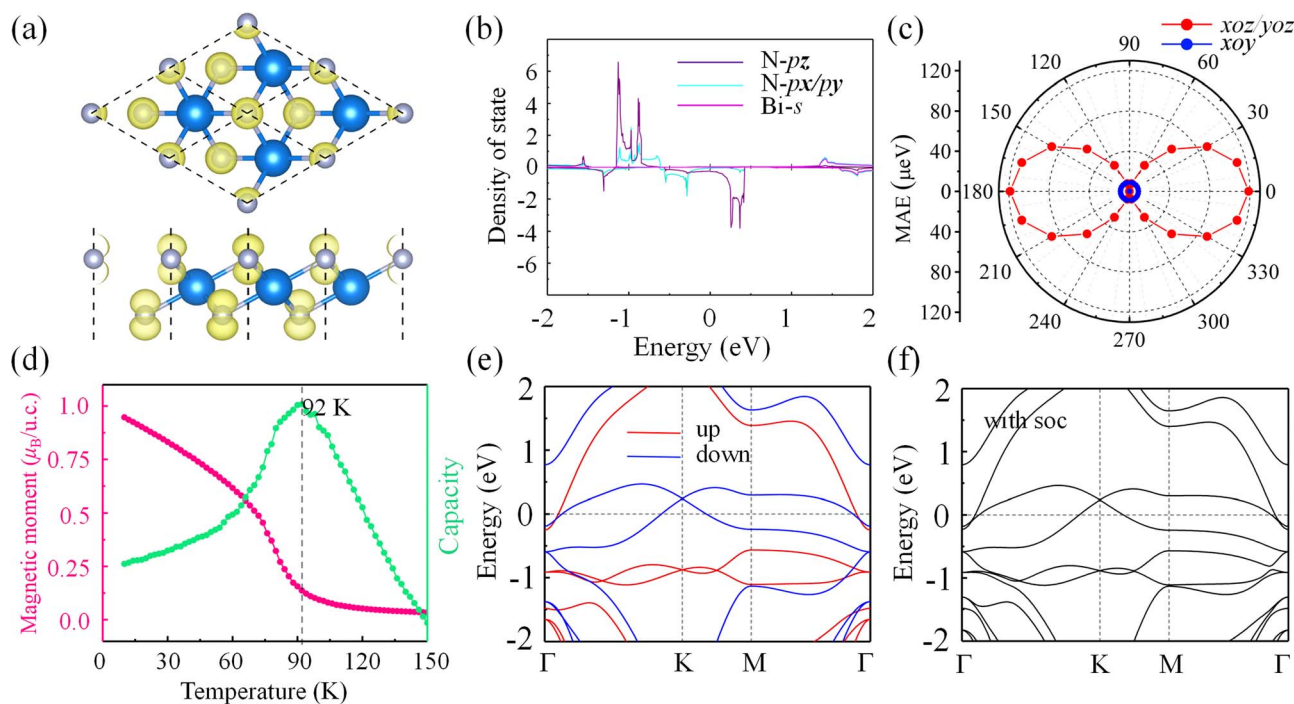

Fig. 2 Magnetic properties of T-BiN$_2$. (a) The spin density distribution for monolayer T-BiN$_2$. (b) Projected density of states diagram, with different colored lines representing atomic orbital contributions. (c) Angular dependence of MAE in the polar coordinate system for monolayer T-BiN$_2$. (d) The magnetic moment and heat capacity with temperature for T-BiN$_2$. Spin-polarized energy band diagram of T-BiN$_2$ in the ferromagnetic state without SOC effect (e) and with SOC effect (f).

Paper

indicates that the magnetism primarily originates from the p orbitals of nitrogen.

To further investigate the magnetic properties of monolayer T-XN$_2$, we constructed a $2 \times 2 \times 1$ supercell and designed three different magnetic configurations, as shown in Fig. S3 in SI. Using the formula $\Delta E = (E_{AFM} - E_{FM})/4$, with the ferromagnetic state as the reference phase, we compared the total energies between different magnetic configurations. It was found that the ground state of monolayer T-XN$_2$ is ferromagnetic, while the antiferromagnetic state is higher than the ferromagnetic state by 50–110 meV per unit cell, indicating that the ferromagnetic state has good stability.

The total magnetic anisotropy energy (MAE) includes contributions from the magnetocrystalline anisotropy (MCA) and the magnetic dipole–dipole anisotropy energy, and the dipole–dipole anisotropy energy contribution can be significant for large-scale systems. In this work we only consider MCA with SOC effect and have treated MCA as the MAE.[33,34] We have calculated the MAE under the effect of SOC, which describes the magnetic properties of monolayer T-BiN$_2$, as shown in Fig. 2(c). We define the MAE as the MAE $= E_{100} - E_{001}$, where E_{100} and E_{001} represent the total energy of ferromagnetic states along [100] and [001] direction. It can be observed that, due to the equivalent energies along the x and y directions, the angular dependence in the x_{oz} plane resembles that in the y_{oz} plane. Numerically, the magnetization direction tends to favor the out-of-plane direction, with an energy lower that is 118.7 μeV lower than that of the in-plane orientation.

The key parameter of ferromagnetic spintronic devices is the Curie temperature (T_C), which can be obtained using Monte Carlo simulations based on the Heisenberg model. Its Hamiltonian can be expressed as:[35]

$$H = -J_1 \sum_{i,j} S_i \cdot S_j - J_2 \sum_{i,j} S_i \cdot S_j + A \sum_i (S_i^z)^2 \quad (2)$$

where the S represent the magnetic moment, the subscripts i and j label the N sites, J_1 and J_2 are the nearest-neighbor and next-nearest-neighbor coupling parameters, and A represents MAE, respectively. Using the above parameters, J_1 and J_2 can be obtained, and their expressions are as follows:

$$E_{FM} = E_0 - \frac{1}{2}(3J_1 + 6J_2)S^2 \quad (3)$$

$$E_{AFM1} = E_0 - \frac{1}{2}(J_1 - 2J_2)S^2 \quad (4)$$

$$E_{AFM1} = E_0 - \frac{1}{2}(-J_1 - 2J_2)S^2 \quad (5)$$

$$J_1 = \frac{E_{AFM2} - E_{FM}}{S^2} \quad (6)$$

$$J_2 = -\frac{E_{AFM2} + E_{FM} - 2E_{AFM1}}{4S^2} \quad (7)$$

All relevant magnetic parameters of monolayer T-XN$_2$ are listed in Table 2. The results show that the Curie temperatures of T-SbN$_2$ and T-BiN$_2$ are 155 K and 92 K, respectively, which are lower than those of their counterparts T-PN$_2$ at 385 K and T-AsN$_2$ at 460 K.[21,22]

Strain engineering is commonly used to manipulate the physical properties of materials, such as magnetism, band structure, topological properties and superconductivity of two-dimensional materials.[36,37] In this study, we investigate the effect of in-plane biaxial strain on magnetism. Strain ε can be written as $\varepsilon = (a/a_0 - 1) \times 100\%$, where a and a_0 represent the lattice constants after and before stretching, respectively. Here, we focuses on the magnetic properties within the strain range of -5% to 5%. Fig. 3(a) and (e) illustrates the variation of the magnetic moment of monolayer T-SbN$_2$ and T-BiN$_2$ under different strains. It is evident that under the compressive strain, the magnetic moment remains unchanged at 1 μ_B, while it continuously increases with the increase in tensile strain, reaching 1.07 μ_B (SbN$_2$) and 1.13 μ_B (BiN$_2$) at 5%. The total energy changes with strain for different magnetic configurations are shown in Fig. 3(b) and (f). The calculated results indicate that for monolayer T-SbN$_2$, the ferromagnetic state remains the ground state, regardless of whether it is under tensile or compressive strain. Similarly, monolayer T-BiN$_2$ is also ferromagnetic within the strain range we calculated. According to the trend of total energy changes shown in Fig. 3(f), with the continuous increase of compressive strain, monolayer T-BiN$_2$ may transition from a ferromagnetic state to a antiferromagnetic state.

The variation of the Curie temperature of the ferromagnet with in-plane biaxial strain is shown in Fig. 3(d) and (h). For the monolayer T-SbN$_2$ and T-BiN$_2$, the response curves of the Curie temperature to strain are nearly monotonic; monolayer T-SbN$_2$ shows a monotonically decreasing trend, while monolayer T-BiN$_2$ exhibits a monotonically increasing trend. Both are quite sensitive to strain, with a variation range reaching 100–200 K. This change is mainly due to the effect of strain on the magnetic nearest-neighbor coupling parameters, as illustrated in the Fig. 3(c) and (g). The trends in the magnetic nearest-neighbor coupling constant align with the variations in the Curie temperature, and this pattern also exists in the two-dimensional ferromagnetic materials MnN and XN.[38] Considering the limited impact of strain on magnetic MAE, the energy difference between the antiferromagnetic and ferromagnetic spin ordered structures induced by strain represents the effective coupling interaction between adjacent magnetic atoms.[39] For monolayers T-SbN$_2$ and T-BiN$_2$, this is almost the sole response to structural deformation (the bond length between adjacent magnetic atoms).

Compared to strain engineering, the use of an electrolyte gate can more easily achieve carrier (hole or electron) doping in
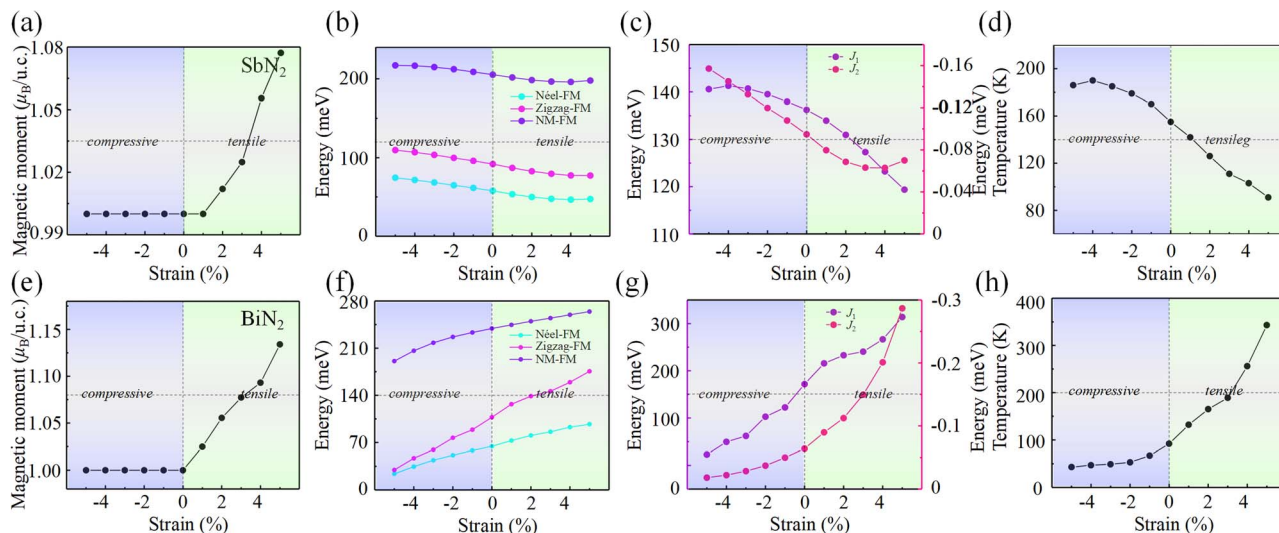
Table 2 In this work, we calculated the magnetic-related parameters, including the total energy difference (ΔE (meV)), magnetic nearest-neighbor coupling parameters (J_1 (meV), J_2 (μeV)), MAE (μeV), and ferromagnetic Curie temperature (T_C (K))

Materials	$\Delta E_{N'eel}$	ΔE_{zigzag}	ΔE_{stripe}	J_1	J_2	MAE	T_C
T-SbN$_2$	57.7	71.2	91.8	136.4	0.095	97.5	155
T-BiN$_2$	64.5	83.1	107.4	171.7	−0.064	118.7	92

Fig. 3 Magnetic properties as a function of strain. The magnetic moment as a function of biaxial strain for T-SbN$_2$ (a) and T-BiN$_2$ (e). The total energy difference of the magnetic configuration as a function of biaxial strain for T-SbN$_2$ (b) and T-BiN$_2$ (f). The magnetic coupling parameters J_1 and J_2 as a function of biaxial strain for T-SbN$_2$ (c) and T-BiN$_2$ (g). The ferromagnetic Curie temperature as a function of biaxial strain for T-SbN$_2$ (d) and T-BiN$_2$ (h).

experiments, while simulation calculations are conducted by removing or adding electrons within the system.[40,41] Carrier doping can induce Stoner-type ferromagnetic phase transitions in nonmagnetic materials; therefore, we will investigate the influence of carriers on the ferromagnetic properties of monolayers T-SbN$_2$ and T-BiN$_2$. The range of carrier concentration we calculated is $0 - 5 \times 1.01 \times 10^{14}$ (9.47×10^{13}) for T-SbN$_2$ (T-BiN$_2$), which can be extracted or injected experimentally through positive or negative gate voltages, and this concentration range is relatively easy to achieve in experiments. Fig. 4(a) and (e) shows that the magnetic moment of monolayer T-XN$_2$

has an almost linear relationship with carrier concentration, with a slope of 1 μ_B per 1.01×10^{14} (9.47×10^{13}) for T-SbN$_2$ (T-BiN$_2$) concentration, indicating that the doped carriers are fully spin-polarized. Similar to strain engineering, Fig. 4(a) and (e) shows that carrier doping still results in a ferromagnetic ground state for monolayer T-XN$_2$. The difference is that as the electron doping concentration increases, the total energy difference between different magnetic configurations becomes larger, whereas the opposite is true for hole doping. In addition, the ferromagnetic Curie temperature of monolayer T-XN$_2$ varies with carrier concentration as shown in Fig. 4(d) and (h). The
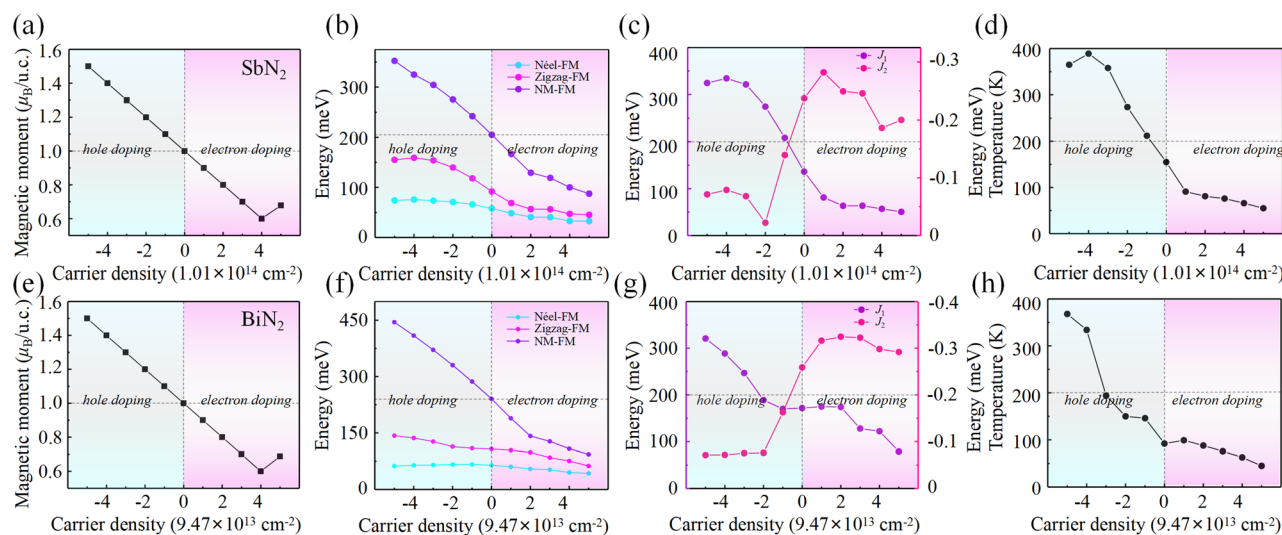

Fig. 4 Magnetic properties as a carrier doping. The magnetic moment as a function of carrier doping for T-SbN$_2$ (a) and T-BiN$_2$ (e). The total energy difference of the magnetic configuration as a function of carrier doping for T-SbN$_2$ (b) and T-BiN$_2$ (f). The magnetic coupling parameters J_1 and J_2 as a function of carrier doping for T-SbN$_2$ (c) and T-BiN$_2$ (g). The ferromagnetic Curie temperature as a function of carrier doping for T-SbN$_2$ (d) and T-BiN$_2$ (h).

trends are generally similar: as the hole concentration increases, the ferromagnetic Curie temperature increases, while an increase in electron concentration leads to a decrease in the ferromagnetic Curie temperature. We also examined the relationship between the magnetic nearest-neighbor coupling constant and carrier concentration. It can be observed that the trend of the magnetic nearest-neighbor coupling constant is almost consistent with that of the ferromagnetic Curie temperature, similar to the effects of strain engineering. Therefore, it can be concluded that carrier doping is one of the effective methods for tuning the magnetic Curie temperature. In summary, monolayer $T\text{-}XN_2$ maintains good ferromagnetism and semimetallic properties under the effects of external biaxial strain and carrier doping.

4   Summary

In summary, we theoretically predicted a metal-free ferromagnet, the V-group nitride $T\text{-}XN_2$ (X = Sb, Bi), which has a structure similar to $T\text{-}MoS_2$ and consists of three atomic layers occupying positions A, B, and C. Based on first-principles calculations, we confirmed its stability from the perspectives of thermodynamics, dynamics, and mechanical properties. Spin-polarized calculations indicated that monolayer $T\text{-}XN_2$ exhibits magnetism, originating from the p orbitals of nitrogen. By comparing the total energies of different magnetic configurations, we found that the ferromagnetic state is the ground state, with Curie temperatures of 155 K ($T\text{-}SbN_2$) and 92 K ($T\text{-}BiN_2$), which are lower than those of the similar $T\text{-}PN_2$ (385 K) and $T\text{-}AsN_2$ (460 K).[21,22] In addition, strain engineering and carrier doping can effectively tune the magnetic properties, demonstrating strong robustness. The above results indicate that monolayer $T\text{-}XN_2$ are a promising metal-free ferromagnet.

Conflicts of interest

There are no conflicts to declare.

Data availability

The data supporting this article are included within the main text or the supplementary information (SI). Additional data are available from the authors upon request. Supplementary information: results of the structural stability and magnetic results of monolayer $T\text{-}BiN_2$. See DOI: https://doi.org/10.1039/d5ra05842b.

Acknowledgements

References

1 B. Wang, Y. Bai, C. Wang, S. Liu, S. Yao, Y. Jia and J. Cho, *Phys. Rev. B*, 2024, **110**, 094423.

2 J. Zhang, Y. Shao, C. Li, J. Xu, H. Zhang, C. Wang, B. Wang and J. Cho, *Appl. Phys. Lett.*, 2024, **125**, 142404.

3 Y. Ren, Z. Qiao and Q. Niu, *Rep. Prog. Phys.*, 2016, **79**, 066501.

4 X. Wang, Z. Song, W. Wen, H. Liu, J. Wu, C. Dang, M. Hossain, M. A. Iqbal and L. Xie, *Adv. Mater.*, 2019, **31**, 1804682.

5 B. Huang, G. Clark, E. Navarro-Moratalla, D. R. Klein, R. Cheng, K. L. Seyler, D. Zhong, E. Schmidgall, M. A. McGuire, D. H. Cobden, et al., *Nature*, 2017, **546**, 270–273.

6 C. Gong, L. Li, Z. Li, H. Ji, A. Stern, Y. Xia, T. Cao, W. Bao, C. Wang, Y. Wang, et al., *Nature*, 2017, **546**, 265–269.

7 M. Kang, L. Ye, S. Fang, J.-S. You, A. Levitan, M. Han, J. I. Facio, C. Jozwiak, A. Bostwick, E. Rotenberg, et al., *Nat. Mater.*, 2020, **19**, 163–169.

8 Y. Deng, Y. Yu, Y. Song, J. Zhang, N. Z. Wang, Z. Sun, Y. Yi, Y. Z. Wu, S. Wu, J. Zhu, et al., *Nature*, 2018, **563**, 94–99.

9 M. Bonilla, S. Kolekar, Y. Ma, H. C. Diaz, V. Kalappattil, R. Das, T. Eggers, H. R. Gutierrez, M.-H. Phan and M. Batzill, *Nat. Nanotechnol.*, 2018, **13**, 289–293.

10 J.-J. Zhang, L. Lin, Y. Zhang, M. Wu, B. I. Yakobson and S. Dong, *J. Am. Chem. Soc.*, 2018, **140**, 9768–9773.

11 G. Liu, C. Zhen, Y. Kang, L. Wang and H.-M. Cheng, *Chem. Soc. Rev.*, 2018, **47**, 6410–6444.

12 I. Choudhuri, P. Bhauriyal and B. Pathak, *Chem. Mater.*, 2019, **31**, 8260–8285.

13 A. V. Rozhkov, A. L. Rakhmanov, A. O. Sboychakov, K. I. Kugel and F. Nori, *Phys. Rev. Lett.*, 2017, **119**, 107601.

14 S. Sanvito, *Chem. Soc. Rev.*, 2011, **40**, 3336–3355.

15 Q. Yang, W. Xiong, L. Zhu, G. Gao and M. Wu, *J. Am. Chem. Soc.*, 2017, **139**, 11506–11512.

16 S. Wang, H. Ge, S. Sun, J. Zhang, F. Liu, X. Wen, X. Yu, L. Wang, Y. Zhang, H. Xu, et al., *J. Am. Chem. Soc.*, 2015, **137**, 4815–4822.

17 Y. Wang and Y. Ding, *J. Mater. Chem. C*, 2016, **4**, 7485–7493.

18 H. Chen, L. Yan, X.-l. Wang, J.-j. Xie, J. Lv and H.-s. Wu, *ACS Omega*, 2024, **9**, 1389–1397.

19 J. Liu, Z. Liu, T. Song and X. Cui, *J. Mater. Chem. C*, 2017, **5**, 727–732.

20 J. Ding, Q. Yao, H. Sun, S. Chen, F. Wu, C. Huang and E. Kan, *J. Mater. Chem. C*, 2021, **9**, 14401–14407.

21 Q. Zhang, Y. Zhang, Y. Li, D. Fang, J. Che, E. Zhang, P. Zhang and S. Zhang, *Phys. Chem. Chem. Phys.*, 2022, **24**, 7077–7083.

22 P. Zhao, Q. Wang, J. Ru and Y. Liang, *Appl. Phys. Lett.*, 2023, **123**, 163105.

23 P. Hohenberg and W. Kohn, *Phys. Rev.*, 1964, **136**, B864.

24 W. Kohn and L. J. Sham, *Phys. Rev.*, 1965, **140**, A1133.

25 G. Kresse and J. Furthmüller, *Comput. Mater. Sci.*, 1996, **6**, 15–50.

26 G. Kresse and J. Furthmüller, *Phys. Rev. B: Condens. Matter Mater. Phys.*, 1996, **54**, 11169.

27 J. P. Perdew, K. Burke and M. Ernzerhof, *Phys. Rev. Lett.*, 1996, **77**, 3865–3868.

28 P. Giannozzi, S. de Gironcoli, P. Pavone and S. Baroni, *Phys. Rev. B: Condens. Matter Mater. Phys.*, 1991, **43**, 7231–7242.

29 V. Wang, N. Xu, J.-C. Liu, G. Tang and W.-T. Geng, *Comput. Phys. Commun.*, 2021, **267**, 108033.

30 Z.-j. Wu, E.-j. Zhao, H.-p. Xiang, X.-f. Hao, X.-j. Liu and J. Meng, *Phys. Rev. B: Condens. Matter Mater. Phys.*, 2007, **76**, 054115.

31 A. Togo and I. Tanaka, *Scr. Mater.*, 2015, **108**, 1–5.

32 D. Bucher, L. C. Pierce, J. A. McCammon and P. R. Markwick, *J. Chem. Theory Comput.*, 2011, **7**, 890–897.

33 C. Jin, C. Liu, F. Ren, B. Wang, M. Jia and Q. Gu, *Appl. Phys. Lett.*, 2023, **123**, 262902.

34 C. Jin, C. Liu, F. Ren, B. Wang, M. Jia, H. Shen, X. Liu and Q. Gu, *J. Appl. Phys.*, 2025, **138**, 064504.

35 Y. Zhang, B. Wang, Y. Guo, Q. Li and J. Wang, *Comput. Mater. Sci.*, 2021, **197**, 110638.

36 A. Rodin, A. Carvalho and A. Castro Neto, *Phys. Rev. Lett.*, 2014, **112**, 176801.

37 X.-H. Peng, S. Ganti, A. Alizadeh, P. Sharma, S. K. Kumar and S. K. Nayak, *Phys. Rev. B: Condens. Matter Mater. Phys.*, 2006, **74**, 035339.

38 I. V. Solovyev, P. H. Dederichs and V. I. Anisimov, *Phys. Rev. B: Condens. Matter Mater. Phys.*, 1994, **50**, 16861–16871.

39 W. Xiong, B. Lei, Y. Gao, R. Yang, A. Li and F. Ouyang, *Results Phys.*, 2024, **60**, 107665.

40 Y. Lu, J.-Y. Wang and J. Pei, *Acc. Chem. Res.*, 2021, **54**, 2871–2883.

41 J. Euvrard, Y. Yan and D. B. Mitzi, *Nat. Rev. Mater.*, 2021, **6**, 531–549.